

Lawrence Berkeley National Laboratory

LBL Publications

Title

Large exciton binding energy in a bulk van der Waals magnet from quasi-1D electronic localization

Permalink

<https://escholarship.org/uc/item/2qs7715k>

Journal

Nature Communications, 16(1)

ISSN

2041-1723

Authors

Smolenski, Shane

Wen, Ming

Li, Qiuyang

et al.

Publication Date

2025

DOI

10.1038/s41467-025-56457-x

Copyright Information

This work is made available under the terms of a Creative Commons Attribution License, available at <https://creativecommons.org/licenses/by/4.0/>

Peer reviewed

Large exciton binding energy in a bulk van der Waals magnet from quasi-1D electronic localization

Received: 2 April 2024

Accepted: 21 January 2025

Published online: 29 January 2025

 Check for updates

Shane Smolenski¹, Ming Wen², Qiuyang Li¹, Eoghan Downey¹, Adam Alfrey³, Wenhao Liu⁴, Aswin L. N. Kondusamy⁵, Aaron Bostwick⁶, Chris Jozwiak⁶, Eli Rotenberg⁶, Liuyan Zhao¹, Hui Deng¹, Bing Lv^{4,5}, Dominika Zgid^{1,2}, Emanuel Gull¹ & Na Hyun Jo¹✉

Excitons, bound electron-hole pairs, influence the optical properties in strongly interacting solid-state systems and are typically most stable and pronounced in monolayer materials. Bulk systems with large exciton binding energies, on the other hand, are rare and the mechanisms driving their stability are still relatively unexplored. Here, we report an exceptionally large exciton binding energy in single crystals of the bulk van der Waals antiferromagnet CrSBr. Utilizing state-of-the-art angle-resolved photoemission spectroscopy and self-consistent *ab-initio* *GW* calculations, we present direct spectroscopic evidence supporting electronic localization and weak dielectric screening as mechanisms contributing to the amplified exciton binding energy. Furthermore, we report that surface doping enables broad tunability of the band gap offering promise for engineering of the optical and electronic properties. Our results indicate that CrSBr is a promising material for the study of the role of anisotropy in strongly interacting bulk systems and for the development of exciton-based optoelectronics.

Excitons are energetically favorable bound states of excited electrons and holes with an energy less than the single-particle (electronic) band gap. This energy difference between the exciton energy and the electronic gap is the exciton binding energy. Since excitons are bound by the Coulomb interaction, the binding energy can primarily be enhanced by weak dielectric screening and charge localization^{1–8}. Strong interactions, manifested by large exciton binding energies, can stabilize excitons up to room temperature⁹ and enhance the associated emergent phenomena, such as exciton condensates¹⁰ and charged excitons¹¹. In addition to stabilization, large binding energies lead to enhanced absorption, sharp spectral emission, and electrical tunability¹², all of which are promising properties for next-generation optoelectronic applications,

including photovoltaics¹³ and single photon emitters¹⁴. These large exciton binding energies are most prevalent in monolayer materials, namely monolayer transition metal dichalcogenides (TMDs) where binding energies exceed 500 meV, because of reduced dielectric screening and geometrical confinement^{1,4,7–9}. Bulk materials, with significantly stronger screening environments, typically host excitons with binding energies orders of magnitude lower⁴ yet would provide a platform on which to explore the role of dimensionality in many-body interactions. In theory, bulk materials with strong Coulomb interactions encouraged by anisotropy could overcome this limitation^{15,16}. Particularly, van der Waals magnets, in which anisotropy is necessary to stabilize magnetic order down to the 2D limit¹⁷ and which host exotic quasiparticle interactions¹⁸, could thus provide

¹Department of Physics, University of Michigan, Ann Arbor, MI, USA. ²Department of Chemistry, University of Michigan, Ann Arbor, MI, USA. ³Applied Physics Program, University of Michigan, Ann Arbor, MI, USA. ⁴Department of Physics, The University of Texas at Dallas, Richardson, TX, USA. ⁵Department of Materials Science and Engineering, The University of Texas at Dallas, Richardson, TX, USA. ⁶Advanced Light Source, Lawrence Berkeley National Laboratory, Berkeley, CA, USA. ✉e-mail: nhjo@umich.edu

promising materials in which to detect tightly bound bulk excitons and explore their rich many-body physics.

Among 2D magnets, CrSBr stands out as a highly promising candidate due to its strong optical response and pronounced anisotropy. CrSBr is a van der Waals antiferromagnet that crystallizes in the orthorhombic space group $Pmmn$ (space group number 59) with lattice parameters $a = 3.50 \text{ \AA}$, $b = 4.75 \text{ \AA}$, and $c = 7.94 \text{ \AA}$ near $T = 200 \text{ K}$ ^{19,20}. Its structure is comprised of van der Waals layers in the ab plane with each layer consisting of two buckled CrS sheets capped by Br (Fig. 1a). The corresponding Brillouin zone is shown in Fig. 1b. Below the bulk Néel temperature $T_N = 132 \text{ K}$, CrSBr develops A -type antiferromagnetic (AFM) order where the Cr magnetic moments couple ferromagnetically within the ab plane but antiferromagnetically in the stacking direction with the b -axis being the easy axis^{19,21}. The monolayer has also been proven to remain stable in air and exhibits ferromagnetic ordering within the plane below 146 K ^{20,22}. Moreover, an extraordinary phase transition, which is indicative of weak interlayer coupling, has been revealed in bulk CrSBr where the surface transitions into the AFM state at 140 K while the bulk transitions at 132 K ²³. Importantly, CrSBr exhibits a large optical response arising from Wannier excitons with binding energies predicted to be between $500\text{--}900 \text{ meV}$ for the monolayer^{24,25}. Correspondingly, a large exciton-photon coupling strength of $\sim 20 \text{ meV}$ per monolayer was measured in 2D CrSBr polaritons²⁶. Coupling between charge, spin, and lattice further demonstrates the presence of rich quasi-particle interactions^{24–28}. Alongside structural and magnetic anisotropy, calculations and electrical transport measurements suggest that the electronic structure exhibits strong electronic anisotropy in the form of a quasi-one-dimensional (quasi-1D) conduction band^{25,29}. This is also well captured by our self-consistent GW (sc GW) calculation on monolayer CrSBr shown in Fig. 1c. From these optical and computational results, it has been suggested that CrSBr hosts tightly-bound quasi-1D excitons^{24,25,30}. However, direct experimental observation of these remarkable excitonic properties and their underlying mechanisms has not yet been realized.

In this study, we report the direct measurement of an exceptionally large exciton binding energy in single crystals of CrSBr through angle-resolved photoemission spectroscopy (ARPES) and optical measurements. We attribute the large binding energy to strong charge localization due to electronic and structural anisotropy as well as enhanced Coulomb interactions from diminished dielectric

screening, confirming the inferences from optical and computational results. To our knowledge, this is the first direct measurement of a large exciton binding energy in a 2D magnet. We also demonstrate that the introduction of surface dopants can reduce the band gap and thus tune the electronic and optical properties. Through our study, we shed light on the role of anisotropy in the stabilization and tunability of many-body interactions in bulk excitonic materials.

Results

To evaluate the exciton binding energy, we must compare the electronic gap (E_g , the energy necessary to separately create an electron and a hole) with the optical gap (E_o , the energy necessary to create a bound electron-hole pair). We first investigated the optical gap through reflection and photoluminescence (PL) measurements. At 40 K , both reflection and PL data show strong, narrow features and reveal the optical gap to be 1.362 eV (Fig. 1d and Supplementary Note 1). The good agreement between the PL and reflection data suggests that we are probing the direct transition at Γ .

We next explored the electronic gap by performing ARPES measurements on single crystals of CrSBr. Figure 2a, b show the band dispersion of pristine CrSBr at $T = 192 \text{ K}$ along the high symmetry directions $\Gamma - X$ and $\Gamma - Y$, respectively. Note that high symmetry points are designated based on photon energy scans and iso-energy plots at high binding energies (Supplementary Note 2). The relatively high temperature was chosen to avoid charging effects seen below T_N although low-temperature measurements confirm that the key features do exist at lower temperatures as well (Supplementary Note 3). The shape of the band structure along the high symmetry directions is in strong agreement with previously published ARPES data³¹ and our sc GW calculations (Fig. 2e, f). All of these results corroborate the insulating nature of the material, as evidenced by the lack of intensity at the Fermi level E_F . It should be noted that while our calculations predict a valence band maximum (VBM) at Γ , we do not immediately observe this in the ARPES data due to matrix element effects in the first Brillouin zone³¹. However, the maximum at Γ can be observed in the second Brillouin zone and we thus determine the VBM to be at an energy of 1.84 eV below E_F (Supplementary Note 4). Since we do not observe the conduction band in our pristine samples, this implies that the electronic gap is greater than 1.84 eV . The minimum gap size estimate of 1.84 eV is derived from high-temperature data, which does not exhibit the charging issues present at lower temperatures.

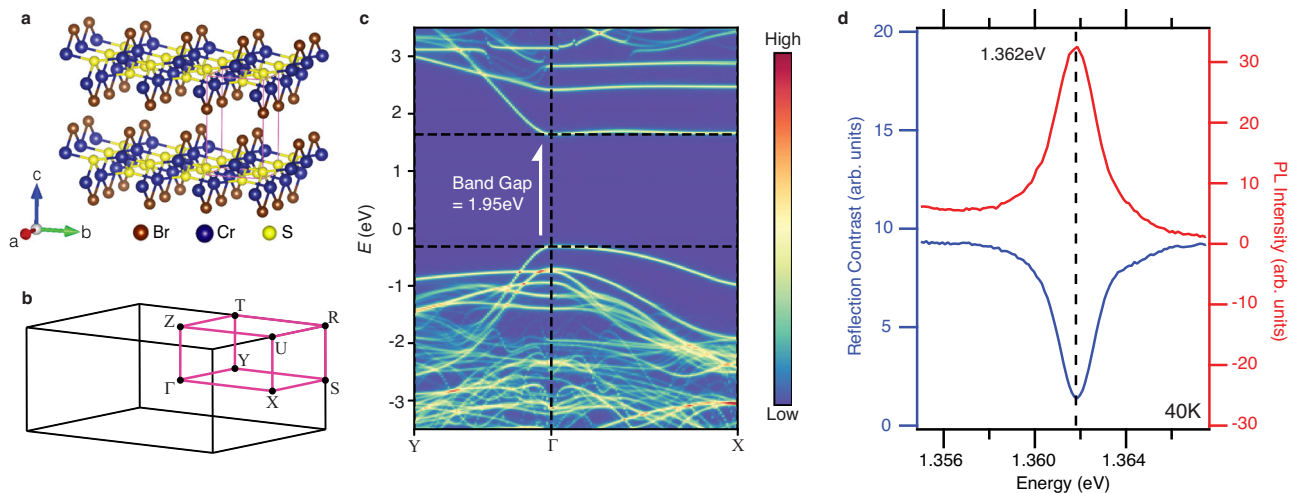


Fig. 1 | Structural, electronic, and optical properties of CrSBr. a Three-dimensional representation of the real-space crystal structure of CrSBr, created with the VESTA software package⁶⁹. The pink rectangular prism represents the unit cell. **b** The corresponding Brillouin zone of CrSBr with high symmetry points

labeled. **c** Self-consistent GW calculations of the electronic band structure of monolayer CrSBr along high symmetry directions in the Γ XSY plane. **d** Reflection contrast and photoluminescence spectra of bulk CrSBr at 40 K . Features in the two spectra are in excellent agreement, revealing an optical gap at Γ of 1.362 eV .

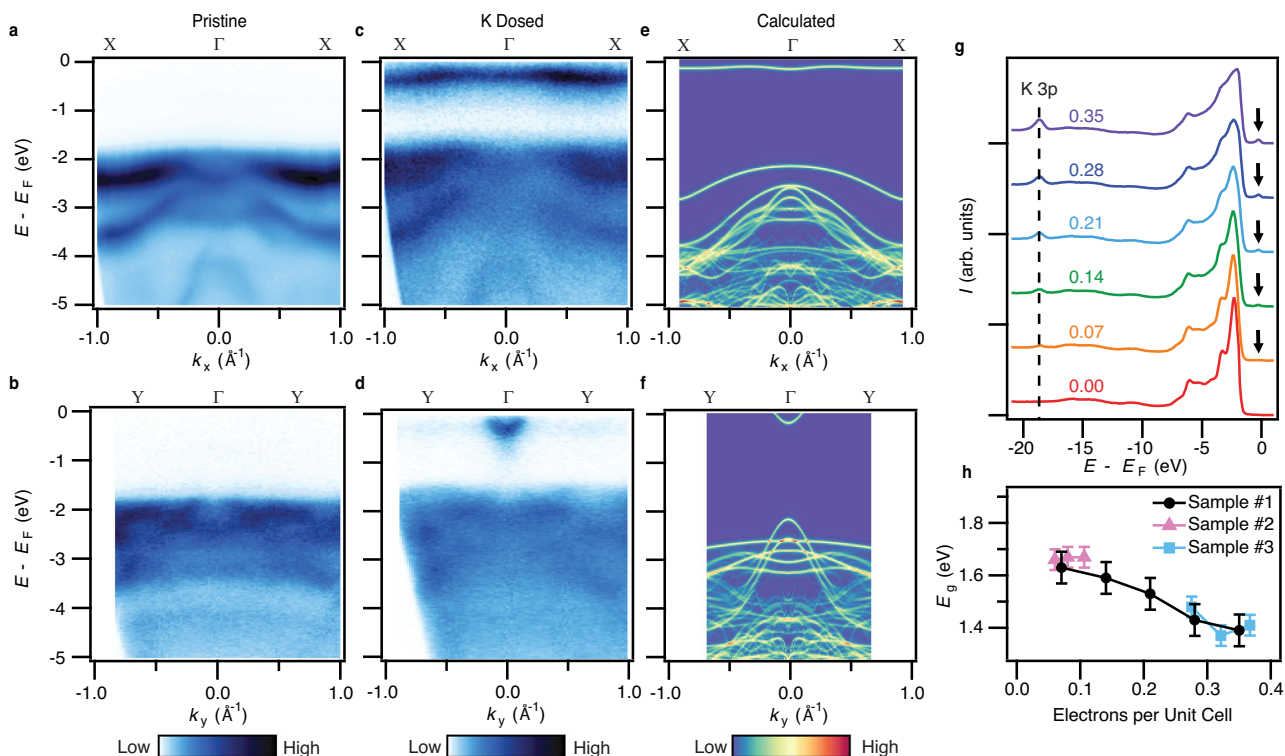


Fig. 2 | Direct visualization of the quasi-1D conduction band and electronic gap.

Experimental band dispersion along the Γ -X and Γ -Y high symmetry lines for (a, b) pristine and (c, d) highly dosed (0.35 electrons per unit cell) bulk CrSBr at $T = 192$ K (paramagnetic regime without charging effects). The emergence of the conduction band and upward energy shift of the valence band upon dosing are evident. scGW calculations of monolayer CrSBr along the (e) Γ -X and (f) Γ -Y. g Energy dispersion curves (EDCs) as a function of K dosing detail the gradual

emergence of conduction band as a function of K dosing, highlighted by the arrows. The numbers above each spectrum corresponds to the dosing level in units of electrons per unit cell. The downward shift in energy of the conduction band along with the upward shift of the valence bands results in a reduction of the band gap as a function of K dosing (h). Error bars indicate estimated error in determining peak positions from the EDCs.

Importantly, however, low-temperature measurements are able to demonstrate that this lower bound (i.e. minimum possible value) on the electronic band gap does not decrease at either 97 K or 40 K (Supplementary Note 3) and that changes to the band structure are minor, in agreement with theory²⁵. This establishes the electronic gap to exceed 1.84 eV at 40K. This measure of the lower bound on the electronic gap is larger than the gap of 1.5 ± 0.2 eV found with scanning tunneling spectroscopy (STS)^{21,25} and contains significantly less uncertainty. Additionally, previous bulk ARPES measurements found the VBM to be at 1.51 eV below E_F , also with no observation of the conduction band, and thus established 1.51 eV as a lower bound of the electronic gap³¹. Yet, due to significant charging at low temperatures, the authors speculated that the gap is likely much larger than 1.51 eV³¹. Our ARPES measurements are able to establish a larger lower bound on the electronic gap because our sample is heavily n-doped, as evidenced through comparison to our calculations. This eliminates (or significantly reduces) charging effects in our samples (Supplementary Note 5). This n-doping arises from our growth procedure where the high vapor pressure helps reduce halide vacancies.

Because our sample is heavily n-doped, we expect the conduction band to be just above E_F . Therefore, it is likely that the conduction band can be detected through in-situ alkali metal surface doping (dosing), a procedure expected to donate electrons to the system, thus raising the Fermi level and causing a rigid downward energy shift of the bands. Using potassium (K) as our dopant, we performed five rounds of dosing to reach a surface dopant density of 0.35 electrons per unit cell (Supplementary Notes 6 and 7). The successful dosing of K is confirmed through the growth of the K 3p core peak at -19 eV below E_F , as shown by the vertical dashed line in Fig. 2g. More importantly, a

feature arises at E_F upon dosing, highlighted by the black arrows in Fig. 2g. To explore this feature more closely, we present the high symmetry band dispersion along Γ -X and Γ -Y for fully dosed (0.35 electrons per unit cell) bulk CrSBr in Fig. 2c, d. In the dosed samples we observe a band near E_F that is nearly flat along k_x , but highly dispersive along k_y . By comparing the dispersion to our scGW calculations, we conclude that this feature is the conduction band and not from other sources such as degenerate defect states. We observe that the experimental band gap is indirect, as the conduction band minimum is located at the X point, -50 meV lower than at Γ (Supplementary Note 8). Note that, despite the indirect gap, the dominant optical response is due to the transition at Γ ^{24,32}. Additionally, we observe that, besides broadening, the shapes of the valence bands remain qualitatively similar upon K dosing but that the energy of the top valence band has increased while the energies of the lower valence bands remain roughly unchanged. As the conduction band shifts downward while the valence band shifts upward, we necessarily observe a reduction in the band gap as a function of K dosing (Fig. 2h). This evolution diverges from the expected rigid downward band movement and fixed band gap.

Discussion

Thus, our ARPES experiments have unveiled three notable findings: (1) a substantial band gap exceeding 1.84 eV; (2) a highly anisotropic conduction band; and (3) an anomalous evolution in the band gap upon K dosing. We now explore the implications of each of these observations. First, it is evident that CrSBr hosts tightly bound excitons. Comparing the values of E_0 to the lower bound of E_g extracted from our ARPES data, we establish the exciton binding energy

($E_b = E_g - E_o$) in single crystal CrSBr to be greater than 478 meV. An exciton binding energy of this magnitude is significantly larger than other bulk inorganic semiconductors^{1,4,8,33–44}, including bulk TMDs (Fig. 3). Rather, this lower bound on the exciton binding energy

roughly follows the universal trend of monolayer semiconductors where $E_b = \frac{1}{4}E_g$ ⁴⁵, suggestive of the strong van der Waals character of bulk CrSBr.

To explore the physical mechanisms for this exceptionally large bulk exciton binding energy, we examine the evolution of the electronic structure upon K dosing. First, we analyze the significant anisotropy of the conduction band to understand charge localization. Figure 4a presents the iso-energy plot in the Γ XY plane at an energy corresponding to the conduction band at Γ (0.29 eV below E_F). The presence of a single stripe-like feature that is extended along k_x and truncated along k_y directly confirms the in-plane anisotropic nature of the conduction band. This feature is in excellent agreement with our scGW calculation (Fig. 4b). Additionally, we observe a stripe-like feature extended along k_z and truncated along k_y , indicating a relatively flat conduction band along the k_z direction (Supplementary Note 7). From these observations along with Fig. 2c, d, it is evident that the conduction band exhibits quasi-1D characteristics. While such quasi-1D nature has been theoretically predicted and inferred through electrical transport and optical measurements^{24,25,29}, this presents the first direct, momentum- and energy-resolved confirmation of the quasi-1D electronic structure in bulk CrSBr.

We quantify this observed anisotropy by fitting the peaks of the energy dispersion curves (EDCs) along $\Gamma - X$ and $\Gamma - Y$ to extract the effective mass of the electrons in the vicinity of Γ (Fig. 4c). We report experimental electron effective masses of $m_x^* = 12.26 m_e$ (3.58 m_e , calculated) and $m_y^* = 0.48 m_e$ (0.22 m_e , calculated), where m_e is the free electron mass. These values correspond to an effective mass ratio of $\frac{m_x^*}{m_y^*} = 25.63$ (16.43, calculated). The discrepancy between experimental and calculated values is likely due to strong correlation effects outside the scope of our calculations. This effective mass anisotropy is large, even among other known quasi-1D materials⁴⁶. Notably, the mass anisotropy is significantly greater than previous reports of $\frac{m_x^*}{m_y^*} = 6.50$ in exfoliated CrSBr⁴⁷, likely due to substrate effects in exfoliated CrSBr. Furthermore, calculations reveal significant anisotropy in the valence band as well with hole effective masses of $m_x^* = 3.75 m_e$ and $m_y^* = 0.17 m_e$ which correspond to a ratio of $\frac{m_x^*}{m_y^*} = 22.32$.

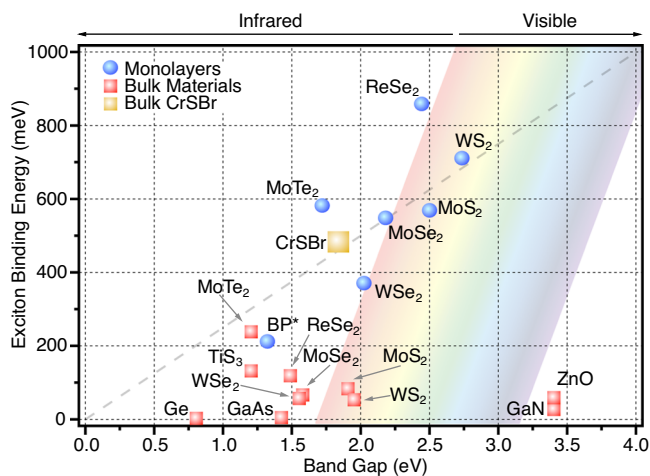


Fig. 3 | Large exciton binding energy of CrSBr in comparison to other inorganic bulk semiconductors. Plot of the exciton binding energy versus the electronic band gap for various monolayer and bulk semiconductors^{1,4,8,33–44}. For the bulk TMDs, the gap at the K point (which is the relevant transition for the excitons) is plotted instead of the indirect gap. For all the other materials, the direct band gaps are used. For CrSBr, the gap plotted is the lower bound on the direct electronic gap found through our pristine ARPES measurements. The rainbow background represents the spectrum of the exciton energy (optical gap) for a given electronic gap and exciton binding energy. Notably, bulk materials have an exciton binding energy below 250 meV except for bulk CrSBr, which has a binding energy similar to those for monolayer TMDs. The gray dashed-line plots the $E_b = \frac{1}{4}E_g$ trend for monolayer semiconductors⁴⁵ which bulk CrSBr roughly obeys. All data points are from experimental works. The measurements for anisotropic black phosphorous (BP) were performed on a bilayer, hence the asterisk.

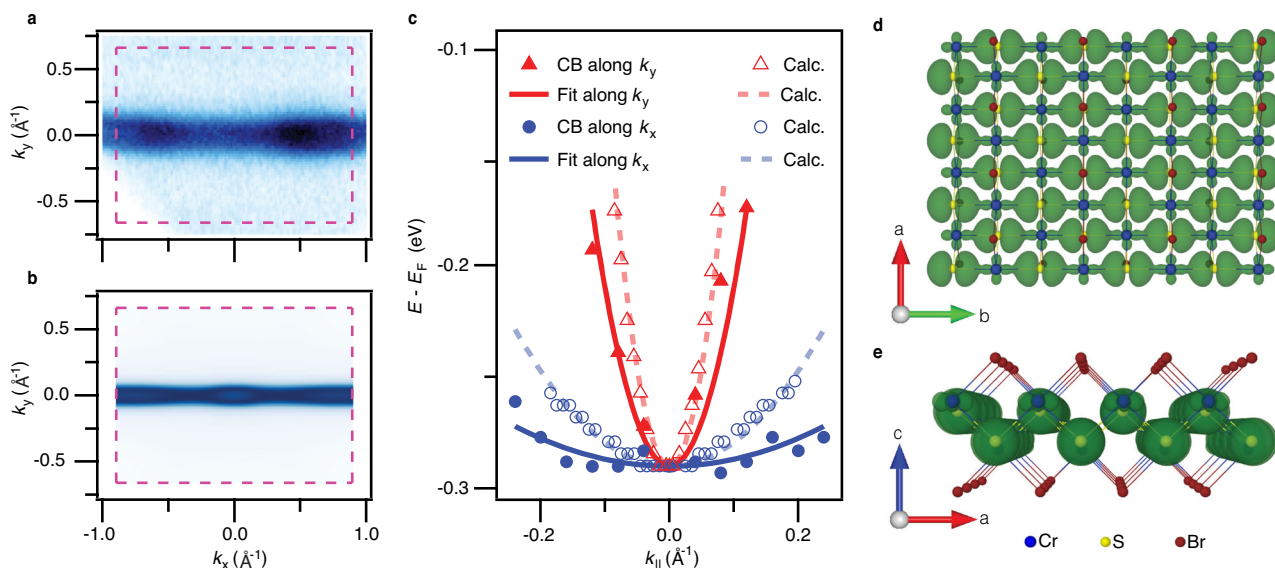


Fig. 4 | Charge localization arising from the quasi-1D conduction band. **a** Experimental iso-energy plot in the Γ XY plane at the conduction band energy at Γ taken at $T = 192\text{K}$ (Paramagnetic regime). **b** Calculated iso-energy plots in the Γ XY plane at the conduction band minimum. The stripe-like feature is indicative of a quasi-1D electronic structure. **c** Experimental (solid markers and lines) and calculated (empty markers and dashed lines) energy dispersion of the CB along $\Gamma - X$ and

$\Gamma - Y$ lines. The markers are band positions found from peak positions of the EDCs. The lines are quadratic fits to the peak positions. The calculated curves have been offset in energy to match the position of the experimental data. scGW calculations of the spatial extent of the dominant orbitals of the bottom conduction band and top valence band viewed along the **(d)** c - and **(e)** b -axes. The electrons are localized in 1D chains along the b -axis.

This effective mass anisotropy in both the conduction and valence bands is indicative of localization of the charge carriers. To confirm this charge localization, we calculated the real-space densities of the dominant orbitals comprising the lowest conduction and highest valence band (Fig. 4d, e). We observe a strong charge localization along the crystallographic *b*-axis, consistent with previous calculations²⁵ and our observations in the electronic structure. We thus confirm the robust confinement of charge carriers along 1D channels in bulk CrSBr. Crucially, spatial confinement, typically arising from geometric origins, is known to enhance exciton binding energy in van der Waals semiconductors^{1,4,5,7}. Therefore, we argue that the charge localization arising from the quasi-1D electronic structure contributes to the tightly bound excitons observed here in CrSBr. Notably, this localization arises from electronic anisotropy, potentially offering insight into the mechanisms enabling the existence of tightly bound excitons in a bulk material.

We next examine the anomalous evolution of the electronic band structure upon K dosing. From Fig. 2a–d, it is clear that in the K-dosed dispersion the conduction band has shifted downward in energy while the valence band has shifted upward, relative to the pristine bands. By measuring the conduction and valence band positions as a function of K dosing, we track this evolution more closely (Supplementary Note 7). We observe that the conduction band suddenly appears after the first dosing round (0.07 electrons per unit cell). It then proceeds to shift only slightly downward in energy upon further dosing. In contrast, the valence band initially shifts downward before gradually moving upward. Importantly, we observe a significant reduction in the direct gap at Γ from greater than 1.84 eV down to 1.65 eV at a dosing level of 0.07 electrons per unit cell before a roughly linear reduction down to 1.39 eV at 0.35 electrons per unit cell (Fig. 2h). This tunability of the band gap with K dosing is consistent within multiple samples.

We now discuss the physical explanations for this anomalous behavior. We first rule out the possibility of negative electronic compressibility (NEC), a decrease of the Fermi level upon an increase in carrier density, as we do not observe an upward energy shift in neither the deep valence bands nor the core levels⁴⁸ (Fig. 2a–d, g and the traces for Sample 1 in Supplementary Fig. 6). Additionally, the evolution cannot be explained by the intercalation of K atoms as the K 3*p* core peak maintains its sharp line shape throughout the entire dosing process⁴⁹ (Supplementary Note 7). Instead, we propose that the anomalous band evolution and reduction of the gap are most likely due to carrier-induced band gap renormalization (BGR) and the surface Stark effect (SSE).

First, BGR is a well-documented effect where the introduction of free carriers alters the screening environment and causes a sharp decrease in the electronic gap^{50,51}. Notably, this effect is theorized to be most pronounced for low doping levels and for a high density of states of the free carriers⁵¹. Indeed, our data demonstrate a large band gap reduction upon light K dosing and the quasi-1D nature of the conduction band supports a large electronic density of states. Furthermore, previous ARPES studies on low-dimensional CrSBr exfoliated on Au and Ag report band gaps of only 1.14 and 1.18 eV⁴⁷, respectively, which, we argue, is suggestive of substrate-induced BGR. Similar to the addition of free carriers, a substrate can drastically alter the screening environment of exfoliated flakes, reducing electron-electron interactions and causing a sharp drop in the electronic gap. The observation of this substrate-induced effect suggests that the analogous carrier-induced BGR may also be observed in CrSBr. Additionally, a similar evolution of the valence and conduction bands has been observed in K-dosed WS₂/h-BN where the increase in screening from the filling of the conduction band is found to be responsible for the band renormalization⁵². This is consistent with our BGR description of the band renormalization we observe in CrSBr. Thus, we ascribe the sudden emergence of the conduction band and immediate decrease in gap size to carrier-induced BGR.

The linear upward shift in the valence band and the resultant reduction in band gap for dosing levels greater than 0.07 electrons per unit cell can then be explained by the SSE (Fig. 2h and Supplementary Note 7). The SSE is a phenomenon whereby a vertical electric field localizes the conduction and valence electrons at different potentials in real space which results in a renormalization of the band gap^{53,54}. Notably, this effect has been thoroughly demonstrated in alkali metal-dosed van der Waals materials^{44,55} where the ionized alkali metal atoms on the surface are responsible for the vertical electric field. Furthermore, previous theoretical work has demonstrated that an external vertical electric field applied to CrSBr is capable of creating the strong real-space separation of the conduction and valence electrons necessary to produce the SSE⁵⁶. Additionally, the band gap reduction from the SSE is expected to be linear as a function of electric field for large fields^{53,54}, in agreement with our ARPES data (Fig. 2h). We also note that competition between the chemical potential shift and the SSE has been previously reported and can explain the initial downward movement of the valence band⁵⁵.

Importantly, large contributions from both carrier-induced BGR and SSE are indicative of weak dielectric screening and strong 2D character^{44,50–52,57}. This strong 2D character and related weak screening observed in bulk samples of CrSBr can be understood through the highly anisotropic electronic structure. In tandem with the formation of in-plane quasi-1D chains of electron density, weak interlayer coupling driven by the orbital contents of the lowest energy conduction band and highest energy valence band contributes to out-of-plane localization. Specifically, these bands have minimal contribution from Br orbitals (<10% Br any orbital, <5% Br *p_z*) throughout the Brillouin zone, as deduced from our *scGW* calculations (Supplementary Note 9) and visible in Fig. 4d, e. Since Br atoms form capping layers on each van der Waals sheet, the lack of Br *p_z* orbital contribution results in weakened interlayer coupling and, consequently, out-of-plane localization and reduced screening²⁵. Compared to MoS₂, a TMD with weak contributions from S *p_z* orbitals near Γ (<6%) but significant contributions near Γ (28%)⁵⁸, CrSBr demonstrates even weaker interlayer coupling and thus the electronic properties are less affected by the inclusion of additional layers, enabling weak screening even in the bulk. Crucially, weak dielectric screening strengthens Coulomb interactions and has been shown to contribute significantly to large exciton binding energies in 2D materials^{2–8}. Thus, the large observed exciton binding energy in bulk CrSBr can be further explained by weak dielectric screening arising from the anisotropic electronic structure. Additional experiments exploring the effects of doping and externally-applied electric fields can further establish the role of BGR and SSE in CrSBr.

We therefore determine that bulk CrSBr hosts tightly bound excitons due to quasi-1D charge localization and weak dielectric screening. The key role of the anisotropy, both structural and electronic, provides optimism that large exciton binding energies can be found in other highly anisotropic bulk van der Waals systems. Particularly, other van der Waals magnets, where predictions of extraordinarily large exciton binding energies in CrBr₃, CrI₃, and MnPS₃ have already been made^{6,59}, could provide additional systems in which to study the dimensionality of excitons. The band gap tunability upon surface doping also presents a method to easily adjust the electronic and optical properties of CrSBr, an effect that opens possibilities for both the further study of many-body physics and the development of semiconductor devices.

Methods

Crystal growth

CrSBr single crystals were synthesized via the direct solid-vapor method following the one we described before²⁰. Chromium powder (Cr, Alfa Aesar, 99.97%), sulfur powder (S, Alfa Aesar, 99.5%), and solidified Br₂ were loaded into a clean quartz ampoule in an atomic molar ratio of 1:1.1:1.2, then sealed under vacuum using a liquid

nitrogen trap. The sealed ampoule was gradually heated to 930 °C, maintained at this temperature for 20 hours, and then slowly cooled to 750 °C at a rate of 1 °C per hour followed by the furnace cooling to room temperature. Large CrSBr single crystals formed naturally at the bottom of the ampoule, while a small amount of CrBr₃ appeared at the top of the ampoule and was easily separated from the CrSBr crystals.

Optical measurements

Reflection contrast (RC) and photoluminescence (PL) spectroscopies were conducted by real-space imaging of the sample. The sample was kept in a Montana Fusion system for temperature control. An objective lens with a numerical aperture (NA) of 0.42 was used for both focusing and collection. A supercontinuum white light laser (NKT Photonics, SuperK) with a beam size of $\sim 2\ \mu\text{m}$ in diameter was used as the white-light source for RC measurements. A continuous-wave solid-state laser at 532 nm with a power of 100 μW and a beam size of $\sim 2\ \mu\text{m}$ in diameter was used as a pump for PL measurements. The collected signals were detected by a Princeton Instruments spectrometer with a cooled charge-coupled camera.

ARPES measurements

All ARPES measurements were performed at Beamline 7.0.2 (MAESTRO) of the Advanced Light Source. The beamline is equipped with a R4000 spectrometer with deflectors that enable data collection across the full Brillouin zone without moving the sample. Bulk CrSBr crystals were mounted on Cu pucks with Epotek H20E silver epoxy and cleaved in situ at vacuum better than 5×10^{-11} mbar. All measurements with fixed photon energy were performed with 83–84 eV photons with linear horizontal polarization. The beam spot size was $15\ \mu\text{m} \times 15\ \mu\text{m}$. Paramagnetic measurements were performed at temperatures of 192K, 195K, and 195K for Sample 1, Sample 2, and Sample 3, respectively while antiferromagnetic measurements (Supplementary Note 3) were performed on Sample 1 at a temperature of 97K and on a fourth sample at roughly 40K (Supplementary Note 3). Potassium dosing experiments were performed by evaporating potassium onto the cleaved CrSBr surface in situ from a SAES getter source such that the sample was not moved from the measurement position. The level of potassium adsorption was estimated using Luttinger's theorem (Supplementary Note 6).

Self-consistent GW calculations

Self-consistent GW calculations were performed on the Matsubara axis using a finite-temperature Gaussian-orbital based self-consistent Green's function solver^{60–62}. Calculations used the gth-szv-molopt-sr basis set⁶³ with the gth-pbe pseudopotential⁶⁴.

Self-consistent GW iterations were initialized with a density functional calculation using the PBE functional⁶⁵, using the `pyscf`⁶⁶ software package, and iterated to self-consistency.

Results were converged on the Matsubara axis using convergence acceleration⁶⁷. Results were then analytically continued to the real frequency axis using Nevanlinna analytical continuation⁶⁸.

The results shown here are obtained in a monolayer geometry using a periodic k -space mesh of size $6 \times 8 \times 1$. Supporting Materials present additional details regarding the symmetrized atomic orbital decomposition, charge density calculation, and 2-D density of state iso-energy surface.

Data availability

Relevant data for the work are available at the Deep Blue Repositories: DOI: 10.7302/8rxk-b929. Further information are available from the corresponding author upon reasonable request.

Code availability

The MIT-licensed open source code GREEN is available at <https://doi.org/10.5281/zenodo.12541090>.

References

1. Dvorak, M., Wei, S.-H. & Wu, Z. Origin of the variation of exciton binding energy in semiconductors. *Phys. Rev. Lett.* **110**, 016402 (2013).
2. Latini, S., Olsen, T. & Thygesen, K. S. Excitons in van der Waals heterostructures: The important role of dielectric screening. *Phys. Rev. B* **92**, 245123 (2015).
3. Regan, E. C. et al. Emerging exciton physics in transition metal dichalcogenide heterobilayers. *Nat. Rev. Mater.* **7**, 778 (2022).
4. Zhang, G. et al. Determination of layer-dependent exciton binding energies in few-layer black phosphorus. *Sci. Adv.* **4**, eaap9977 (2018).
5. Thygesen, K. S. Calculating excitons, plasmons, and quasiparticles in 2D materials and van der Waals heterostructures. *2D Mater.* **4**, 022004 (2017).
6. Birowska, M., Junior, P. E. F., Fabian, J. & Kunstmann, J. Large exciton binding energies in MnPS₃ as a case study of a van der Waals layered magnet. *Phys. Rev. B* **103**, L121108 (2021).
7. Zheng, X. & Zhang, X. Excitons in two-dimensional materials. *Advances in Condensed-Matter and Materials Physics-Rudimentary Research to Topical Technology* (2019).
8. Jung, E. et al. Unusually large exciton binding energy in multi-layered 2H-MoTe₂. *Sci. Rep.* **12**, 4543 (2022).
9. Mueller, T. & Malic, E. Exciton physics and device application of two-dimensional transition metal dichalcogenide semiconductors. *npj 2D Mater. Appl.* **2**, 29 (2018).
10. Wang, Z. et al. Evidence of high-temperature exciton condensation in two-dimensional atomic double layers. *Nature* **574**, 76 (2019).
11. Ross, J. S. et al. Electrical control of neutral and charged excitons in a monolayer semiconductor. *Nat. Commun.* **4**, 1474 (2013).
12. Ross, J. S. et al. Electrically tunable excitonic light-emitting diodes based on monolayer WSe₂ p-n junctions. *Nat. Nanotechnol.* **9**, 268 (2014).
13. Bernardi, M., Palumbo, M. & Grossman, J. C. Extraordinary sunlight absorption and one nanometer thick photovoltaics using two-dimensional monolayer materials. *Nano Lett.* **13**, 3664 (2013).
14. Koperski, M. et al. Single photon emitters in exfoliated WSe₂ structures. *Nat. Nanotechnol.* **10**, 503 (2015).
15. Sharma, A. et al. Highly enhanced many-body interactions in anisotropic 2D semiconductors. *Acc. Chem. Res.* **51**, 1164 (2018).
16. Balandin, A. A., Kargar, F., Salguero, T. T. & Lake, R. K. One-dimensional van der Waals quantum materials. *Mater. Today* **55**, 74 (2022).
17. Mermin, N. D. & Wagner, H. Absence of ferromagnetism or antiferromagnetism in one- or two-dimensional isotropic Heisenberg models. *Phys. Rev. Lett.* **17**, 1133 (1966).
18. Jiang, X. et al. Recent progress on 2D magnets: Fundamental mechanism, structural design and modification. *Appl. Phys. Rev.* **8** (2021).
19. Göser, O., Paul, W. & Kahle, H. Magnetic properties of CrSBr. *J. Magn. Magn. Mater.* **92**, 129 (1990).
20. Liu, W. et al. A three-stage magnetic phase transition revealed in ultrahigh-quality van der Waals bulk magnet CrSBr. *ACS Nano* **16**, 15917 (2022).
21. Telford, E. J. et al. Layered antiferromagnetism induces large negative magnetoresistance in the van der Waals semiconductor CrSBr. *Adv. Mater.* **32**, 2003240 (2020).
22. Lee, K. et al. Magnetic order and symmetry in the 2D semiconductor CrSBr. *Nano Lett.* **21**, 3511 (2021).
23. Guo, X. et al. Extraordinary phase transition revealed in a van der Waals antiferromagnet. *Nat. Commun.* **15**, 6472 (2024).
24. Wilson, N. P. et al. Interlayer electronic coupling on demand in a 2D magnetic semiconductor. *Nat. Mater.* **20**, 1657 (2021).
25. Klein, J. et al. The bulk van der Waals layered magnet CrSBr is a quasi-1D material. *ACS Nano* **17**, 5316 (2023).

26. Li, Q. et al. Two-dimensional magnetic exciton polariton with strongly coupled atomic and photonic anisotropies. *Phys. Rev. Lett.* **133**, 266901 (2024).
27. Lin, K. et al. Strong exciton–phonon coupling as a fingerprint of magnetic ordering in van der Waals layered CrSBr. *ACS Nano* **18**, 2898–2905 (2024).
28. Cenker, J. et al. Reversible strain-induced magnetic phase transition in a van der Waals magnet. *Nat. Nanotechnol.* **17**, 256 (2022).
29. Wu, F. et al. Quasi-1D electronic transport in a 2D magnetic semiconductor. *Adv. Mater.* **34**, 2109759 (2022).
30. Wang, T. et al. Magnetically-dressed CrSBr exciton-polaritons in ultrastrong coupling regime. *Nat. Commun.* **14**, 5966 (2023).
31. Bianchi, M. et al. Paramagnetic electronic structure of CrSBr: Comparison between ab initio GW theory and angle-resolved photoemission spectroscopy. *Phys. Rev. B* **107**, 235107 (2023).
32. Tabataba-Vakili, F. et al. Doping-control of excitons and magnetism in few-layer CrSBr. *Nat. Commun.* **15**, 4735 (2024).
33. Saigal, N., Sugunakar, V. & Ghosh, S. Exciton binding energy in bulk MoS₂: A reassessment. *Appl. Phys. Lett.* **108** (2016).
34. Beal, A., Knights, J. & Liang, W. Transmission spectra of some transition metal dichalcogenides. II. Group VIA: trigonal prismatic coordination. *J. Phys. C: Solid State Phys.* **5**, 3540 (1972).
35. Beal, A. & Liang, W. Excitons in 2H-WSe₂ and 3R-WSe₂. *J. Phys. C: Solid State Phys.* **9**, 2459 (1976).
36. Arora, A. et al. Excitonic resonances in thin films of WSe₂: from monolayer to bulk material. *Nanoscale* **7**, 10421 (2015).
37. Nam, S. et al. Free-exciton energy spectrum in GaAs. *Phys. Rev. B* **13**, 761 (1976).
38. Macfarlane, G., McLean, T., Quarrington, J. & Roberts, V. Exciton and phonon effects in the absorption spectra of germanium and silicon. *J. Phys. Chem. Solids* **8**, 388 (1959).
39. Arora, A. et al. Highly anisotropic in-plane excitons in atomically thin and bulklike 1T'-ReSe₂. *Nano Lett.* **17**, 3202 (2017).
40. Molina-Mendoza, A. J. et al. Electronic bandgap and exciton binding energy of layered semiconductor TiS₃. *Adv. Electron. Mater.* **1**, 1500126 (2015).
41. Klots, A. et al. Probing excitonic states in suspended two-dimensional semiconductors by photocurrent spectroscopy. *Sci. Rep.* **4**, 6608 (2014).
42. Yang, J. et al. Robust excitons and trions in monolayer MoTe₂. *ACS Nano* **9**, 6603 (2015).
43. Wang, G. et al. Colloquium: Excitons in atomically thin transition metal dichalcogenides. *Rev. Mod. Phys.* **90**, 021001 (2018).
44. Kang, M. et al. Universal mechanism of band-gap engineering in transition-metal dichalcogenides. *Nano Lett.* **17**, 1610 (2017).
45. Jiang, Z., Liu, Z., Li, Y. & Duan, W. Scaling universality between band gap and exciton binding energy of two-dimensional semiconductors. *Phys. Rev. Lett.* **118**, 266401 (2017).
46. Jin, Y., Li, X. & Yang, J. Single layer of MX₃ (M = Ti, Zr; X = S, Se, Te): A new platform for nano-electronics and optics. *Phys. Chem. Chem. Phys.* **17**, 18665 (2015).
47. Bianchi, M. et al. Charge transfer induced Lifshitz transition and magnetic symmetry breaking in ultrathin CrSBr crystals. *Phys. Rev. B* **108**, 195410 (2023).
48. Wen, W., Zhao, G., Hong, C., Song, Z. & He, R.-H. 3D negative electronic compressibility as a new emergent phenomenon. *J. Supercond. Nov. Magn.* **33**, 229 (2020).
49. Riley, J. M. et al. Negative electronic compressibility and tunable spin splitting in WSe₂. *Nat. Nanotechnol.* **10**, 1043 (2015).
50. Faridi, A., Culcer, D. & Asgari, R. Quasiparticle band-gap renormalization in doped monolayer MoS₂. *Phys. Rev. B* **104**, 085432 (2021).
51. Gao, S. & Yang, L. Renormalization of the quasiparticle band gap in doped two-dimensional materials from many-body calculations. *Phys. Rev. B* **96**, 155410 (2017).
52. Katoch, J. et al. Giant spin-splitting and gap renormalization driven by trions in single-layer WS₂/h-BN heterostructures. *Nat. Phys.* **14**, 355 (2018).
53. Khoo, K. & Louie, S. G. et al. Tuning the electronic properties of boron nitride nanotubes with transverse electric fields: A giant DC Stark effect. *Phys. Rev. B* **69**, 201401 (2004).
54. Ramasubramaniam, A., Naveh, D. & Towe, E. Tunable band gaps in bilayer transition-metal dichalcogenides. *Phys. Rev. B* **84**, 205325 (2011).
55. Kim, J. et al. Observation of tunable band gap and anisotropic Dirac semimetal state in black phosphorus. *Science* **349**, 723 (2015).
56. Dang, W. et al. Electric-field-tunable spin polarization and carrier-transport anisotropy in an A-type antiferromagnetic van der Waals bilayer. *Phys. Rev. Appl.* **18**, 064086 (2022).
57. Xiong, P.-Y., Chen, S.-Z., Zhou, W.-X. & Chen, K.-Q. Semiconductor-metal transition induced by giant Stark effect in blue phosphorene nanoribbons. *Phys. Lett. A* **381**, 2016 (2017).
58. Cappelluti, E., Roldán, R., Silva-Guillén, J., Ordejón, P. & Guinea, F. Tight-binding model and direct-gap/indirect-gap transition in single-layer and multilayer MoS₂. *Phys. Rev. B-Condens. Matter Mater. Phys.* **88**, 075409 (2013).
59. Grzeszczyk, M. et al. Strongly correlated exciton-magnetization system for optical spin pumping in CrBr₃ and CrI₃. *Adv. Mater.* **35**, 2209513 (2023).
60. Iskakov, S., Yeh, C.-N., Gull, E. & Zgid, D. Ab initio self-energy embedding for the photoemission spectra of NiO and MnO. *Phys. Rev. B* **102**, 085105 (2020).
61. Yeh, C.-N., Iskakov, S., Zgid, D. & Gull, E. Fully self-consistent finite-temperature GW in Gaussian Bloch orbitals for solids. *Phys. Rev. B* **106**, 235104 (2022).
62. Iskakov, S. et al. Green/weakcoupling: Implementation of fully self-consistent finite-temperature many-body perturbation theory for molecules and solids. *Comput. Phys. Commun.* **306**, 109380 (2025).
63. VandeVondele, J. & Hutter, J. Gaussian basis sets for accurate calculations on molecular systems in gas and condensed phases. *J. Chem. Phys.* **127**, 114105 (2007).
64. Goedecker, S., Teter, M. & Hutter, J. Separable dual-space gaussian pseudopotentials. *Phys. Rev. B* **54**, 1703 (1996).
65. Perdew, J. P., Burke, K. & Ernzerhof, M. Generalized gradient approximation made simple. *Phys. Rev. Lett.* **77**, 3865 (1996).
66. Sun, Q. et al. PySCF: The Python-based simulations of chemistry framework. *WIREs Comput. Mol. Sci.* **8**, e1340 (2018).
67. Pokhilko, P., Yeh, C.-N. & Zgid, D. Iterative subspace algorithms for finite-temperature solution of Dyson equation. *J. Chem. Phys.* **156**, 094101 (2022).
68. Fei, J., Yeh, C.-N. & Gull, E. Nevanlinna analytical continuation. *Phys. Rev. Lett.* **126**, 056402 (2021).
69. Momma, K. & Izumi, F. VESTA 3 for three-dimensional visualization of crystal, volumetric and morphology data. *J. Appl. Crystallogr.* **44**, 1272 (2011).

Acknowledgements

We are grateful to Kai Sun for insightful discussions. This research was supported by the NSF CAREER grant under Award No. DMR-2337535 and the National Science Foundation (NSF) through the Materials Research Science and Engineering Center at the University of Michigan, Award No. DMR-2309029. This work used resources of the Advanced Light Source, a U.S. Department of Energy (DOE) Office of Science User Facility under Contract No. DE-AC02-05CH11231. Q.L., A.A and H.D. acknowledge the support by the Office of Naval Research Award No. N00014-21-1-2770 and Gordon and Betty Moore Foundation Award No.

GBMF10694. L.Z. acknowledges support by US Air Force Office of Scientific Research (AFOSR) YIP grant no. FA9550-21-1-0065, NSF CAREER grant no. DMR-174774 and Alfred P. Sloan Foundation. The work at UT Dallas is supported by the US Air Force Office of Scientific Research (AFOSR FA9550-19-1-0037), National Science Foundation (NSF-DMREF-2324033), and Office of Naval Research (ONR N00014-23-1-2020 and N00014-22-1-2755).

Author contributions

W.L., A.L.N.K., and B.L. synthesized the single crystal. S.S., E.D., A.B., C.J., E.R., and N.H.J. conducted the ARPES experiment. M.W. performed the scGW calculations. D.Z. and E.G. developed the scGW code and methodology. Q.L., A.A., L.Z., and H.D. helped prepare samples and performed optical measurements. S.S., M.W., Q.L., D.Z., E.G., and N.H.J. wrote the manuscript in consultation with E.D., A.A., W.L., A.L.N.K., A.B., C.J., E.R., L.Z., and H.D.

Competing interests

The authors declare no competing interests.

Additional information

Supplementary information The online version contains supplementary material available at <https://doi.org/10.1038/s41467-025-56457-x>.

Correspondence and requests for materials should be addressed to Na Hyun Jo.

Peer review information *Nature Communications* thanks the anonymous reviewer(s) for their contribution to the peer review of this work. A peer review file is available.

Reprints and permissions information is available at <http://www.nature.com/reprints>

Publisher's note Springer Nature remains neutral with regard to jurisdictional claims in published maps and institutional affiliations.

Open Access This article is licensed under a Creative Commons Attribution-NonCommercial-NoDerivatives 4.0 International License, which permits any non-commercial use, sharing, distribution and reproduction in any medium or format, as long as you give appropriate credit to the original author(s) and the source, provide a link to the Creative Commons licence, and indicate if you modified the licensed material. You do not have permission under this licence to share adapted material derived from this article or parts of it. The images or other third party material in this article are included in the article's Creative Commons licence, unless indicated otherwise in a credit line to the material. If material is not included in the article's Creative Commons licence and your intended use is not permitted by statutory regulation or exceeds the permitted use, you will need to obtain permission directly from the copyright holder. To view a copy of this licence, visit <http://creativecommons.org/licenses/by-nc-nd/4.0/>.

© The Author(s) 2025